Journal of Materials Chemistry C

Meso- to Nano-scopic Domain Structures in High Curie-Temperature Piezoelectric $BiScO_3$-$PbTiO_3$ Single Crystals of Complex Perovskite Structure

Journal:	*Journal of Materials Chemistry C*
Manuscript ID	TC-ART-02-2020-000924.R1
Article Type:	Paper
Date Submitted by the Author:	17-Apr-2020
Complete List of Authors:	Luo, Zeng; Xi'an Jiaotong University Liu, Zenghui; Xi'an Jiaotong University, ; Simon Fraser University , Department of Chemistry Walker, David; University of Warwick, Department of Physics Huband, Steven; University of Warwick, Department of Physics Thomas, Pam; University of Warwick, Department of Physics Zhang, Nan; Xi'an Jiaotong University, a. Electronic Materials Research Laboratory, Key Laboratory of the Ministry of Education & International Center for Dielectric Research Ren, Wei; Xi'an Jiaotong University, Ye, Zuo-Guang; Simon Fraser University, Chemistry

SCHOLARONE™
Manuscripts

Meso- to Nano-scopic Domain Structures in High Curie-Temperature Piezoelectric $BiScO_3$-$PbTiO_3$ Single Crystals of Complex Perovskite Structure

Zeng Luo[1, 2], Zenghui Liu[1, 3, *], David Walker[2], Steven Huband[2], Pam A. Thomas[2], Nan Zhang[1, *], Wei Ren[1], and Zuo-Guang Ye[3, *]

[1] Electronic Materials Research Laboratory, Key Laboratory of the Ministry of Education & International Center for Dielectric Research, Faculty of Electronic and Information Engineering, Xi'an Jiaotong University, Xi'an 710049, China

[2] Department of Physics, University of Warwick, Coventry, West Midlands CV4 7AL, UK

[3] Department of Chemistry and 4D LABS, Simon Fraser University, Burnaby, British Columbia, V5A 1S6, Canada

* Email addresses: zye@sfu.ca, nzhang1@xjtu.edu.cn and liu.z.h@xjtu.edu.cn

Abstract

Bismuth scandate-lead titanate (BS-PT) is of great interest as a promising piezoelectric material for high-temperature electromechanical applications due to its excellent comprehensive electric performance and high Curie temperature. However, the full understanding of the ferro-/piezo-electric properties of BS-PT has been strongly hindered by the lack of detailed investigation of microscopic domain structures and successful growth of high-quality crystals. In this work, detailed structural and meso-/nano-scopic domains studies of the BS-PT

crystals near the morphotropic phase boundary have been carried out by various characterization techniques. The multi-scale domain structures in the <001>$_{cub}$-cut 0.324BS-0.676PT single crystals were investigated by a unique combination of temperature-variable Birefringence Imaging Microscopy and Piezoresponse Force Microscopy, in conjunction with high-resolution X-ray diffraction in the temperature range of 30 - 500 ^{o}C. The crystal was found to exhibit tetragonal symmetry on average at room temperature and showed a transformation to cubic symmetry around 460 ^{o}C. Complex domain structures with small domain sizes (2~6 μm) and a high density of domain walls were imaged and analyzed from meso- to nano-scopic scale, and more interestingly, local crystal distortion was found in the vicinity of the dense domain walls. The domain evolution as a function of temperature and the correlation between the domain structure and the dielectric properties have been studied. These studies of domains, symmetries and phase transitions provide a better understanding of the structure of BS-PT crystals and other related ferro-/piezo-electric single crystals on multiple length scales, and help design novel high-T_C, high performance ferro-/piezo-electric materials.

Keywords: Single crystal, Domain structure, High-resolution X-ray diffraction, Birefringence Imaging Microscopy, Piezoresponse Force Microscopy.

Introduction

Ferroelectric materials with the perovskite structure are of enormous importance for piezoelectric applications such as medical transducers, ultrasonic motors, underwater sonar, and sensors.[1-3] The discovery of the $Pb(Zr_{1-x}Ti_x)O_3$ (PZT) system was a major research breakthrough for technologically useful piezoelectric materials because of its superior piezoelectric properties near the morphotropic phase boundary (MPB), i.e. $x \simeq$ 0.45-0.48.[4] More recently, single crystal of $Pb(Zn_{1/3}Nb_{2/3})O_3$-$PbTiO_3$ (PZNT) and $Pb(Mg_{1/3}Nb_{2/3})O_3$-$PbTiO_3$ (PMNT) have also been actively studied because of their ultra-high piezoelectric coefficients (over 2000 pC/N).[5-7] However, the relatively low ferroelectric Curie temperature (T_C) and the lower MPB phase transition temperature hinder applications of these materials in high-temperature environments. Therefore, considerable effort has been put into searching for high T_C piezoelectric materials. Based on the tolerance factor consideration, Eitel *et al.* prepared (1-*x*)$Bi(Me)O_3$–*x*$PbTiO_3$ solid solutions (where Me^{3+} = Sc, In, Yb, etc.) that show both an MPB and a high Curie temperature.[8] Specifically, the (1-*x*)$BiScO_3$-*x*$PbTiO_3$ (BS-PT) solid solution has attracted a high level of attention both because its electrical properties are comparable to those of PMNT or PZNT, and more importantly, its higher Curie temperature (near the MPB region), than the commercial PZT system (T_C = 386 °C). The BS-PT ceramics exhibit a decent piezoelectric coefficient (d_{33} = 460 pC/ N) with a T_C of 450 °C for compositions near the MPB region. It was also found that the piezoelectric properties of BS-PT were almost temperature

independent up to 400 °C, which indicates that the BS-PT system is a promising candidate for high-temperature electromechanical transducer applications.[8-11]

The phase diagram of BS-PT shows the existence of an MPB region in between the BS-rich rhombohedral side and the PT-rich tetragonal side.[8] Much research has been undertaken to elucidate the MPB nature of the BS-PT system in more detail.[12-14] Temperature-dependent transmission electron microscopy (TEM) results and dielectric measurements confirmed that there was an MPB (x = 0.62-0.65) region bridging the tetragonal and rhombohedral phases.[12] Later, a low-symmetry monoclinic phase was found to coexist with a tetragonal phase in a wider MPB region from x = 0.60 to 0.70.[13] However, the monoclinic-tetragonal MPB was later questioned and the MPB region was suggested to contain two primitive monoclinic lattices (space group P_m).[14] To date, the true symmetries of the MPB phases in the BS-PT system are still under intensive discussion.

So far, most investigations have focused on BS-PT ceramics because of the practical difficulties encountered in growing BS-PT single crystals with high enough quality.[15-18] However, to understand the symmetry and structural features of this system in the MPB region, a comprehensive structural investigation based on high-quality single crystals is essential, which can provide better insights into true nature of the crystal structure. Up to now, only a limited number of studies have been performed on the BS-PT single crystals, principally focusing on the growth methods, the characterization of the electric

properties for practical applications,[19-21] and the conventional structure analysis including crystal lattice parameters, structural symmetry, and so forth.[14, 22] Through the investigation of BS-PT single crystals (x = 0.64), Datta *et al*. showed that the MPB region consisted of two primitive monoclinic lattices (space group *Pm*) via a best fit to high-resolution X-ray data from a twinned crystal.[14] By contrast, the existence of two competing symmetries, *P*4*mm* and *Cm*, together with local disorder was reported in 0.36BS-0.64PT, which was believed to be strongly associated with the high piezoelectric response.[22] Both of their studies mainly focused on the symmetry of the average crystal structure. However, the microstructure and domain structure of BS-PT single crystals, both have an important role in the ferro-/piezo-electricity, but have not been investigated in detail to date.[23] In general, the arrangement and evolution of domains and domain walls play an important role in the functional properties of ferro-/piezo-electric materials, including the dielectric, piezoelectric and ferroelectric properties. For instance, the high permittivity of ferroelectrics widely used in capacitors is dominated by domain wall contributions,[24] and the excellent dielectric and piezoelectric performance of relaxor-based single crystals could be attributed to the presence of nanoscale polar domains.[25]

In this work, multiscale domains in BS-PT crystals have been studied systematically utilizing different methods including birefringence imaging microscopy (BIM) and piezoresponse force microscopy (PFM), together with high-temperature X-ray diffraction. By combining the measurements of the

mesoscopic properties related to the phase transition and the nano-scopic imaging of domains, we reveal the nature of local distortion within the domain wall boundaries and the development of the domains with temperature. Direct insights into the domain configuration and the temperature dependence of tetragonal structure are of significance and may also provide an improved understanding of the dependence of piezoelectricity on the mesoscopic domain structures for the BS-PT crystals, and also for other perovskite MPB piezoelectric crystals.

Experimental

Crystal Growth and Compositional Analysis

Single crystals of (1-*x*)$BiScO_3$-*x*$PbTiO_3$ (BS-PT) were grown using a "top-cooled solution growth'' (TCSG) method. The starting materials of PbO (99.9%), Bi_2O_3 (99.9%), TiO_2 (98%), Sc_2O_3 (99.99%) were selected and weighed according to the required nominal stoichiometry of 0.40BS-0.60PT. They were mixed with a complex flux of (PbO + Bi_2O_3) at an optimized ratio of flux : solute = 6 : 1 in weight. The mixture was thoroughly ground for 0.5 h by hand and then placed into a 50 ml Pt crucible. The details of the growth process were reported previously.[26]

Energy dispersive X-ray spectroscopy (EDX) measurements were performed on the grown crystals together with a scanning electron microscope (FEI, Quanta FEG) to determine the crystal composition.

High-resolution X-ray Diffraction

The orientation of the as-grown pseudo-cubic crystals was confirmed by X-ray diffraction (XRD) carried out on the naturally grown facets of the pseudo-cubic crystals using a PANalytical Empyrean diffractometer employing Cu *Kα*1 radiation. The ground powder of the BS-PT crystals was annealed at 550 °C for 1 h to remove the possible residual stress before XRD measurements. High-resolution powder XRD was performed utilizing a PANalytical X'Pert Pro MPD equipped with a curved Ge (220) Johansson monochromator giving rise to focused Cu *Kα*1 radiation. High-temperature XRD data were collected using an Anton Paar HTK1200N furnace attached to the same diffractometer. The Rietveld refinements[27] of XRD data at room temperature were performed using the TOPAS program.[28]

Birefringence Imaging Microscopy

Birefringence Imaging Microscopy (BIM) with the Metripol system is a useful and unique tool for determining the symmetry of crystals via the evolution of linear birefringence and domain structure with temperature. Detailed descriptions and working principles of this instrument can be found in the literatures.[29-35] The Metripol birefringence measurement system is based upon a rotating polarizer, a circular polarizing analyser and a CCD detector, which is able to track the changes in optical retardation in every pixel (about 1 part in 10^7). The intensity of the transmitted light at each pixel is given by

$$I = \frac{I_0}{2}[1 + sin\,(2\varphi - 2\alpha) sin\delta], \quad (1)$$

where I_0 is the transmitted intensity of the light, φ is the angle measured anticlockwise from the horizontal direction of the microscope stage to the slow (long) axis of the indicatrix, α is the angular position of the analyser as it rotates, and δ is the phase shift introduced to the light passing through a crystal of thickness t and is related to the birefringence Δn according to Eqn. (2):

$$\delta = \frac{2\pi}{\lambda}\Delta n t, \quad (2)$$

where λ is the wavelength of light used. By collecting several images using a CCD detector with varying positions of the polarizer, it is possible to separate the three quantities: I_0, φ and $|\sin\delta|$, and the data are obtained in the form of false-colour images constructed of these quantities. The false-colour image of I_0 normally shows the topography of specimen including the domain structures. The orientation of a section of the optical indicatrix of each corresponding point (pixel) of the single crystal can be obtained in the image of the angle φ. And the phase shift δ corresponds to the difference in length of the ellipse axes and is proportional to retardation, revealing the optical anisotropy, a measure of which can be found in the image of $|\sin\delta|$. It should be noted that a homogeneous crystal shows a single value of the orientation and give a uniform distribution of $|\sin\delta|$. On the other hand, a crystal with complex domain structures displays rich colours in the false-colour image of φ and the orientation distribution varies according to the different domain arrangements.

The phase transitions in the BS-PT single crystals have been studied via the measurement of linear birefringence and observation of domain structure as a

function of temperature varying from room temperature to 500 °C with the help of a heating/cooling stage (LINKAM TP93).

For optical studies, BS-PT crystals of high quality were polished down to a thickness of approximately 100 μm using alumina lapping films. Considering that stresses may affect the ferroelastic domain structures, the samples were annealed in air at 550 °C for 1 h to release the stress arising from the polishing process prior to the optical measurements.

Piezoresponse Force Microscopy

A modified commercial atomic force microscopic system (AFM, Dimension ICON, NanoScope V, Bruker) was used in piezoresponse mode for imaging the static local polar domain structures.[26, 36-39] The crystal was mounted on a piece of silicon with silver paste for Piezoresponse Force Microscopy measurements which were performed in the air at room temperature.

Dielectric measurements

The dielectric properties as a function of temperature was measured from room temperature (RT) to 500 °C at various frequencies with a 4980 Precision LCR meter (Agilent, Hewlett-Packard, USA). A tube furnace (Carbolite) was used to control the temperature.

Results and Discussion

Compositional and Orientational Analyses

To determine the composition and homogeneity of the BS-PT crystals, three

different areas of a $(001)_{cub}$ crystal platelet were chosen for EDX analysis, as shown in Figure 1. The three areas reveal nearly the same patterns, indicating that their compositions are close to each other. The measured atomic fractions for each element and the estimated compositions for the different selected areas are listed in Table 1, together with the calculated average atomic fractions and compositions. Overall, the difference among the three calculated compositions is very small, with the standard deviation for the BS/PT content being 0.008(2), indicating a good homogeneity for the grown BS-PT crystal. The analysis shows that the as-grown single crystals have an actual composition of 0.323(7)BS-0.676(3)PT. When compared with the reported phase diagram, this composition is found to lie in the MPB region (x = 0.60 to 0.70), close to the tetragonal boundary. It is shifted to the PT-rich side of the phase diagram when compared with the nominal composition (0.40BS-0.60PT), which suggests some compositional segregation. This is very common in multi-component solid solution crystal growth because of the different melting points of the starting materials and their different solubility in the flux (PbO and Bi_2O_3).[40] The orientation of the as-grown crystals of pseudocubic morphology was determined by high-resolution X-ray diffraction on the naturally-grown facets obtained from the BS-PT crystal platelets (Figure 2). The $(100)/(001)_{cub}$ and $(200)/(002)_{cub}$ doublets were clearly observed, indicating that the as-grown crystals exhibit the $\{001\}_{cub}$ orientation.

Structural Analysis by X-ray Diffraction and Rietveld Refinement

Temperature variable X-ray powder-diffraction experiments were performed on BS-PT crystals to reveal the temperature-driven structural phase transition. Figure 3(a) shows the XRD patterns recorded in the temperature range between 30 and 500 °C. With increasing temperature, the split peaks of the {200} Bragg reflection gradually merged into a single peak, indicating a structure transition from the tetragonal to a cubic phase.

Rietveld refinements using TOPAS academic software were performed to fit the observed X-ray data. Since the rhombohedral structure gives only a single (200) peak, the possibility of rhombohedral phase was ruled out due to the clear split of the (200) peak in Figure 3(a). The Rietveld refinement results of the representative (100), (110), and (200) pseudocubic diffraction peaks are displayed in Figure 3(b). Clear mismatches can be found when using a single *P*4*mm* model due to the diffuse scattering. Noheda *et al*. suspected that the diffuse scattering in their previous X-ray refinement of PZT solid solution is associated with locally disordered regions in the vicinity of domain walls and proposed a simple method by adding a cubic phase with the *Pm*-3*m* symmetry to improve the agreement between the observed and the calculated profiles without significantly affecting the refined values of the atomic coordinates.[41, 42] Thus, a similar model consisting of a mixture of (*P*4*mm* + *Pm*-3*m*) was tried to refine the XRD pattern. Compared with the refinement using a single space group (*P*4*mm*), the goodness parameters of the refinement using the combined model are significantly improved. The refinement results obtained for the *P*4*mm*

model give R_{exp} = 5.276%, R_{wp} = 18.104%, r_bragg (R_B) = 4.299 and goodness of fit (GOF) = 3.431, while those using the (*P*4*mm* + *Pm*-3*m*) model result in R_{exp} = 5.268%, R_{wp} = 11.211%, R_B = 2.382 for the tetragonal part, and R_B = 4.022 for the cubic part, with GOF = 2.128. (The detailed results on the refinements at RT and 500 °C for these two models can be found in the Supporting Information.) The results of the refinements confirm an average tetragonal symmetry for BS-PT crystal with a composition close to the tetragonal boundary of the MPB region, consistent with the composition analysis. Based on the room-temperature Rietveld refinement results, a mixture of (*P*4*mm* + *Pm*-3*m*) model has been applied for refinements of with various temperature. The dependences of the lattice parameters are given in Fig. 3(c). Upon heating, c/a decreased until 460 °C at which the structure of the BS-PT crystals transforms from the mainly tetragonal phase (with the presence of a small amount of cubic phase) to the high-temperature cubic phase.

Mesoscopic Domain Structures by Birefringence Imaging Microscopy

Figure 4(a) shows the schematic of birefringence imaging microscopy (BIM) set up with the light path. It consists of a rotating polarizer (P_1), a circular analyser (P_2) and a CCD camera. A heating stage is attached to the sample stage for heating/cooling process. The combination of a rotating polarizer and a circular analyser allows separating the intensity of unpolarized light I_0, the phase shift $|\sin\delta|$ and the angle φ.[29, 30] The I_0, $|\sin\delta|$ and φ images obtained by BIM for a $(001)_{cub}$ BS-PT crystal at room temperature are shown in Figure

4(b), (c) and (d). In the false-colour image shown in Figure 4(b), stripe-like domains with a high density which extend throughout almost the whole crystal, except for a small area named A, separated from Part B by a white dotted line in Figure ~~5~~4(b), are clearly observed. In Figure 4(d), only purple and green colours are observed in Area A, based on the colour bar, which indicates that Area A exhibits birefringent domains with optical axes oriented parallel to the $<100>_{cub}$ directions on a $(001)_{cub}$ platelet, i.e. with an extinction angle at 0^o or 90^o to the $<100>_{cub}$ directions. At the same time, the value of $|\sin\delta|$ in Area A is quite high and uniform, as shown in Figure 4(c), indicating a homogeneous tetragonal domain structure. However, in Area B, mutually perpendicular domain bands with a high-density were observed with $(110)_{cub}$ domain walls. Similar domain arrangements have been reported in PMNT50/50 that crystallizes in a tetragonal *P*4*mm* symmetry, corresponding to the so-called *a* domains with polarizations parallel to the [100]/[010] directions.[43] It should be noted that many stripes in Area B having blue or orange colour shown in Figure 4(d) indicate neither 90^o nor 0^o orientation based on the colour bar. And these areas also give a quite low $|\sin\delta|$ value in Part B, which might be caused by the distorted structures in the local regions near domain walls and the domains overlapping along the direction of light propagation.[44] When two or more domains with non-parallel axes of their optical indicatrices overlap each other in the light path, varying colours for both φ and $|\sin\delta|$ images are typically observed. More detailed discussions of local nano-structures are given in the

following section on piezoresponse force microscopy studies.

To study the evolution of the domain structure and phase transition, the changes in the measured $|sin\ \delta|$, the orientation and the distribution of the orientation angles of the specimen were determined as a function of temperature from 200 ^{o}C to 500 ^{o}C by BIM with a heating stage. (Two videos showing the changes of $|sin\ \delta|$ and orientation with temperature are included in the Supporting Information.) Upon the heating process, the crystal was kept stationary with edges parallel to the horizontal direction, i.e. the <100> direction. In order to monitor the domain transformations with temperature in Area A marked in Figure 4(b), a square spot (26×26 in pixel) covering a single domain was chosen, as shown in the schematic image in Figure 5(a). The left-hand column in Figure 5 shows the images of the orientation (Figure 5(a)) in the chosen area measured from 230 ^{o}C to 500 ^{o}C, the distributions of φ (Figure 5(b)) and the average $|sin\ \delta|$ (Figure 5(c)) upon heating. From Figure 5(b) and (c), the average orientation angle of this small area varies by 90^{o} at the temperatures where the $|sin\ \delta|$ signal reaches a minimum. This occurs periodically when δ equals $\pm m\pi$ (m is an integer). The periodic variation stops at around 460 ^{o}C when a phase transition from the tetragonal to cubic phase takes place. The right-hand column including Figure 5(d-f), shows the corresponding Metripol results in Area B in Figure 4(b). Compared with Area A, the domain arrangements in Area B are much more complicated with a smaller domain size of around 6 μm. Since the domain width is very small, a smaller

spot (5×5 in pixel) is chosen to capture the phase transition in a narrow domain band, as shown in Figure 5(d). Figure 5(e) clearly shows the variation of the average orientations of the selected spot in Area B. The angles fluctuate between 110^{o} to 180^{o} at low temperatures. The appearance of non-90^{o} or non-0^{o} angle further confirms the local structural distortion near the domain walls. The fluctuation continues until the temperature reaches 385 ^{o}C where an abnormal change in the orientation occurs: it drops from 180^{o} to nearly 0^{o}. It should be treated with care that such an abrupt change of apparent orientation by 180^{o} is an artefact arising from phase shift. Afterwards the variations of φ and $|sin\ \delta|$ show similar behaviours with those of Area A, demonstrating a tetragonal phase. Overall, the development of domains in Area B indicates that with increasing temperature, the domain walls gradually vanish until the temperature reaches 385 ^{o}C, at which point the multi-domain structure transforms into a homogeneous single-domain state. Both Areas A and B show the tetragonal to cubic phase transition at 460 ^{o}C, indicating a good compositional homogeneity of the crystal.

It is worth noting that the |sinδ|(T) function in Fig. 5(c) is not reaching value 1, as theoretically predicted. This could be explained by two reasons. First, it may be caused by the inhomogeneity arising from the multi-domain state with dense domain walls. In addition, a gradual color change in Part A, as shown in the Supporting Information (video named Ori_1. MP4), was observed near the phase transition temperature, which indicates some local inhomogeneities,

possibley due to defects and/or internal stress. Similar behaviour was also found in the $PbHfO_3$ crystals by Huband *et al.*[35] The second reason might be related to the symmetry. Gupta *et al.* reported a deviation from ideal cubic symmetry in the paraelectric regime of the $K_xNa_{1-x}NbO_3$ crystal based on BIM results.[45] Since the BS-PT crystal also shows a non-zero birefringence in the cubic phase at 500 ^oC, the non-cubic symmetry may subsist above T_C. As a result, the |sinδ|(T) function measured in the selected area in Fig. 5(a) is not reaching value 1.

Nano-Domain Structure by Piezoresponse Force Microscopy

To image and analyze the domains on the nanoscale, high-resolution PFM measurements were undertaken.[37] Figure 6(a) presents the PFM experimental setup. The static local domain structures are imaged by collecting the small signals in response to an external AC field. The displacements of the cantilever are tracked by the reflected laser beam and measured by the signal-processing system. During the PFM measurements, out-of-plane (OOP) phase images are obtained when there is a vertical component of polarization on a $(001)_{cub}$ crystal platelet. For the in-plane (IP) imaging however, the tip of PFM is only sensitive to the lateral component of polarization, which is perpendicular to the scanning direction ($[010]_{cub}$). An as-grown $(001)_{cub}$ facet of BS-PT crystal was chosen for the PFM measurements, in order to avoid the influence of stress caused by polishing, and the overall picture in terms of topography is shown in Figure 6(b).

Figure 7 shows the ferroelastic and static ferroelectric domains of the as-

grown BS-PT crystal imaged by PFM on the local scale. Figures 7(a) and 7(a') are the topographic images of a scanned area of $10 \times 10\,\mu m^2$, showing herringbone domain arrangements. The OOP amplitude and phase images are shown in Figure 7(b) and (c) and the IP amplitude and phase images in Figure 7(d) and (e). From the OOP and IP amplitude images in Figure 7(b) and (d), almost no contrast is seen in the OOP phase but strong contrast in the IP phase. This rules out the possibility of monoclinic crystal symmetry as the polarizations of a monoclinic would lie on the $(110)_{cub}$ plane, which should result in components in both the vertical and lateral modes. This would lead to signals being observed simultaneously in both the OOP and IP phase images, which is not seen here. Corresponding to the topographic image in Figure 7(d), domain stripes with different widths from 2 μm to 3.5 μm are observed in Figure 7(e), showing ferroelastic domain boundaries at 45^o to the [100] direction. It should be noted that adjacent domain stripes give rise to different IP phase responses, as manifested by the different strengths of signal in the IP amplitude, i.e. the brightness of different stripes, as shown in Figure 7(d). As mentioned above, only lateral component of the polarization in the [100] direction can be detected by the cantilever, which means that the domains in bright stripes in Figure 7(d) have polarization along the [100] direction while the domains in the neighbouring stripes may contain the [010] polarization. To prove this deduction, PFM images were taken after rotating the crystal by 90^o, as shown in Figure 7(a'-e'). After the rotation, the OOP amplitude images still show no signal, which

further proves the absence of any vertical component of polarizations. It should be mentioned that the change in the OOP phase is not a physical effect but an artefact of PFM scanning that is caused by a cross-talk between the OOP and IP signals.[36] Clear changes were observed in the IP piezoresponse amplitude and phase images. The bright stripes in Figure 7(d) become dark after rotation, while the dark ones become bright.

The ferroelectric domain structures of the BS-PT crystal are analyzed and discussed in more detail in Figure 8. Figures 8(a) and (b) are the in-plane piezoresponse amplitude and phase images obtained after rotation in Figure 7. As an example, a small area ($2.8 \times 2.8\,\mu m^2$) was selected, as marked with the white square in Figure 8(a) and (b). Figure 8(c) shows schematically the orientations of the spontaneous polarization for the tetragonal phase. The polarizations with upward and downward directions are named as P_{c+} and P_{c-}, the polarizations parallel to the [100] directions are labelled as P_{a1+} and P_{a1-}, and the remaining two polarizations parallel to [010] are called P_{a2+} and P_{a2-}, respectively. The four in-plane polarization vectors are equivalent on the $(001)_{cub}$ plane. Figure 8(d) represents the schematics of the domain structures of the selected area in Figure 8(a). The ferroelectric domains with an average size of about 400 nm in the middle stripe contain the polarization vectors perpendicular to [100], i.e. the $P_{a2+/-}$ components. At the upper-left corner and lower-right corner, the polarizations along the [100] direction are present, as no in-plane phase signal was tracked here. The 180^o ferroelectric domain wall (DW)

and 90° DW between the ferroelastic domains can be clearly observed. It should be mentioned that the real polarization directions depend on the orientation of the crystal. Here, considering the equivalences of P_{a2+} and P_{a2-}, and P_{a1+} and P_{a1-}, direct labels have been used for the purpose of presentation.

The polarizations in the head-to-tail, [110]-oriented, 90° domain boundaries in a tetragonal crystal were believed to be not exactly perpendicular or parallel to the [100] direction, i.e. are “distorted”, as shown in Figure 9(a). The domain-wall thickness was reported to be on nanoscale (around 20 nm).[46, 47] And it should be noted that there is no straightforward way of measuring the actual size of domain walls by PFM due to many factors, like lateral resolution, residual strain and defects. Unlike the ideal domain configuration showed in Figure 9(a), the 90° boundaries in the topographic images (Figure 7(a)) are not linear but wriggled in a region of about 200 ~ 300 nm and their schematics are presented in Figure 9(b), meaning that the local “distortion” may exist in a bigger region rather than within a 20 nm boundary. Moreover, the size of such region is comparable to that of ferroelectric domains (~ 400 nm), but much smaller than the thickness of the crystal platelet (100 μm). Considering that the domain walls will not keep perfectly straight along the direction of light, an overlap of domain boundaries with distortion may exist, forming the obscure areas as shown above in the BIM measurements.

Domain Structures and Dielectric Properties

The domain structure and its thermal evolution in the BS-PT crystals have

been carefully examined and correlated to the dielectric properties of the crystals. Figure 10 shows the variations of the dielectric constant and loss tangent of a (001) BS-PT crystal plate measured at various frequencies as a function of temperature from 20 to 500 °C, together with the domain structures (in the form of orientation images obtained via BIM (200 × 198 μm^2) at selected temperatures. At low temperatures, the crystal exhibits small domains with a high density of domain walls and low dielectric constant and loss. Upon heating above 300 °C, domains start to merge and the domain size increases in some areas where the number of domain walls is reduced dramatically. Interestingly, the dielectric constant and loss at low frequencies show a step-like increase with a strong frequency dispersion, indicating a kind of Maxwell-Wagner relaxation. The Maxwell-Wagner relaxation typically results from the response of charges built up in dielectrics that are inhomogeneous.[48-51] Multi-domain ferroelastic/ferroelectric crystals like BS-PT are inherently inhomogeneous dielectrics where domains and domain walls have different permittivity and conductivity. In addition, local crystal distortion occurs in the vicinity of the dense domain walls and the direction of polarizations inside domain walls is

generally deviated from the ideal polar direction of the tetragonal symmetry in the domains.[52-54] All these heterogeneities create charges that build up on the domain walls. Upon heating, the domains merge and grow in size with the domain walls moving, reorienting and disappearing partially, giving rise to the Maxwell-Wagner relaxation as exhibited in the temperature and frequency dependences of the dielectric constant and loss in Fig. 10. Upon further heating, the domain size increases more significantly before the crystal transforms into the cubic phase at the transition temperature T_C = 460 °C which is marked by the sharp dielectric peak with persistent dispersion.

Conclusions

A detailed investigation is performed on the mesoscopic symmetry and multiscale domain structures of the tetragonal $BiScO_3$-$PbTiO_3$ (BS-PT) crystals with the composition near the MPB region, i.e. 0.324BS-0.676PT. The meso-/nanodomain structures were investigated by using birefringence imaging microscopy (BIM) and piezoresponse force microscopy (PFM) for the first time. High-density ferroelastic domains with a width of 2~6 μm and the overlapping of local region with distorted structures in the vicinity of domain walls are imaged by BIM and PFM. The tetragonal to cubic phase transition temperature (T_C ~ 460 °C) obtained by optical measurements is in a good agreement with

that measured by high-temperature X-ray diffraction. By collecting the variation of optical properties during the heating process, the development of domains and the phase transition were clearly monitored and analyzed, proving that BIM is an effective tool to investigate domain structures. The domain structure and its thermal evolution in the BS-PT crystals have been examined and correlated to the dielectric properties. The combination of various measurements has allowed us to clarify the domain structures, symmetries and phase transition in the tetragonal BS-PT crystals. This comprehensive study provides new insights into investigating multi-scale domains in perovskite piezoelectric crystals with compositions in the MPB region and prompts further understanding on the relationship between local domain structures and properties of the related ferroic materials.

Conflicts of Interest

There are no conflicts to declare.

Acknowledgements

Zeng Luo would like to acknowledge the China Scholarship Council (CSC) for supporting her studies at University of Warwick. The authors would like to thank Prof. A. M. Glazer for helpful discussions. The EDX analysis was carried out at International Center for Dielectric Research (ICDR), Xi'an Jiaotong University, Xi'an, China, with the help of Dr. Yijun Zhang. This work was supported by the National Natural Science Foundation of China (NSFC, Grants No. 61604123 and 51902244), the China Postdoctoral Science Foundation (Grant No.

2018M643632) and the Natural Science Foundation of Shaanxi Province (Grant No. 2019JQ-389). The work at SFU was supported by the U.S. Office of Naval Research (ONR, Grant No. N00014-16-1-3106) and the Natural Sciences and Engineering Research Council of Canada (NSERC, Grant No. 203773).

References

1. S.-E. Park and T. R. Shrout, *Journal of Applied Physics*, 1997, **82**, 1804-1811.
2. K. Uchino, J. Zheng, A. Joshi, Y.-H. Chen, S. Yoshikawa, S. Hirose, S. Takahashi and J. W. C. de Vries, *Journal of Electroceramics*, 1998, **2**, 33-40.
3. S. Zhang, F. Li, X. Jiang, J. Kim, J. Luo and X. Geng, *Progress in Materials Science*, 2015, **68**, 1-66.
4. G. Shirane, K. Suzuki and A. Takeda, *Journal of the Physical Society of Japan*, 1952, **7**, 12-18.
5. D. Viehland, J. Powers, L. E. Cross and J. F. Li, *Applied Physics Letters*, 2001, **78**, 3508-3510.
6. R. Zhang, B. Jiang, W. Cao and A. Amin, *Journal of Materials Science Letters*, 2002, **21**, 1877-1879.
7. K. K. Rajan and L. C. Lim, *Applied Physics Letters*, 2003, **83**, 5277-5279.
8. R. E. Eitel, C. A. Randall, T. R. Shrout, P. W. Rehrig, W. Hackenberger and S.-E. Park, *Japanese Journal of Applied Physics*, 2001, **40**, 5999-6002.

9. P. Seung-Eek and T. R. Shrout, *IEEE Transactions on Ultrasonics, Ferroelectrics, and Frequency Control*, 1997, **44**, 1140-1147.

10. R. E. Eitel, C. A. Randall, T. R. Shrout and S.-E. Park, *Japanese Journal of Applied Physics*, 2002, **41**, 2099-2104.

11. R. E. Eitel, S. J. Zhang, T. R. Shrout, C. A. Randall and I. Levin, *Journal of Applied Physics*, 2004, **96**, 2828-2831.

12. C. A. Randall, R. E. Eitel, T. R. Shrout, D. I. Woodward and I. M. Reaney, *Journal of Applied Physics*, 2003, **93**, 9271-9274.

13. J. Chaigneau, J. M. Kiat, C. Malibert and C. Bogicevic, *Physical Review B*, 2007, **76**, 094111.

14. K. Datta, S. Gorfman and P. A. Thomas, *Applied Physics Letters*, 2009, **95**, 251901.

15. J.-H. Ahn and J.-H. Koh, *Journal of Alloys and Compounds*, 2016, **689**, 138-144.

16. K. Datta, A. Richter, M. Göbbels, D. A. Keen and R. B. Neder, *Physical Review B*, 2016, **93**, 064102.

17. J. Tan and Z. Li, *Journal of Materials Science*, 2016, **51**, 5092-5103.

18. G. Tutuncu, J. S. Forrester, J. Chen and J. L. Jones, *Acta Materialia*, 2017, **137**, 45-53.

19. S. Zhang, L. Lebrun, S. Rhee, R. E. Eitel, C. A. Randall and T. R. Shrout, *Journal of Crystal Growth*, 2002, **236**, 210-216.

20. S. Zhang, C. A. Randall and T. R. Shrout, *Journal of Applied Physics*, 2004, **95**, 4291-4295.

21. S. Zhang, C. A. Randall and T. R. Shrout, *Japanese Journal of Applied Physics*, 2004,

43, 6199-6203.

22. L. Kong, G. Liu, S. Zhang and W. Yang, *Applied Physics Letters*, 2015, **106**, 232901.
23. P. R. Potnis, N.-T. Tsou and J. E. Huber, *Materials*, 2011, **4**, 417-447.
24. A. K. Tagantsev, L. E. Cross and J. Fousek, *Domains in ferroic crystals and thin films*, Springer, 2010.
25. F. Li, S. Zhang, T. Yang, Z. Xu, N. Zhang, G. Liu, J. Wang, J. Wang, Z. Cheng, Z.-G. Ye, J. Luo, T. R. Shrout and L.-Q. Chen, *Nature Communications*, 2016, **7**, 13807.
26. Z. Luo, N. Zhang, Z. Liu, J. Zhuang, J. Zhao, W. Ren and Z.-G. Ye, *Journal of Materials Chemistry C*, 2018, **6**, 9216-9223.
27. H. Rietveld, *Journal of Applied Crystallography*, 1969, **2**, 65-71.
28. A. Coelho, *Journal of Applied Crystallography*, 2005, **38**, 455-461.
29. A. M. Glazer, J. G. Lewis and W. Kaminsky, *Proceedings of the Royal Society of London. Series A: Mathematical, Physical and Engineering Sciences*, 1996, **452**, 2751-2765.
30. M. Geday, J. Kreisel, A. M. Glazer and K. Roleder, *Journal of Applied Crystallography*, 2000, **33**, 909-914.
31. I. G. Wood, P. Daniels, R. H. Brown and A. M. Glazer, *Journal of Physics: Condensed Matter*, 2008, **20**, 235237.
32. A. M. Glazer, N. Zhang, A. Bartasyte, D. S. Keeble, S. Huband and P. A. Thomas, *Journal of Applied Crystallography*, 2010, **43**, 1305-1313.
33. S. Gorfman, A. M. Glazer, Y. Noguchi, M. Miyayama, H. Luo and P. A. Thomas, *Journal of Applied Crystallography*, 2012, **45**, 444-452.

34. S. Gupta, S. Huband, D. S. Keeble, D. Walker, P. Thomas, D. Viehland and S. Priya, *CrystEngComm*, 2013, **15**, 6790-6799.

35. S. Huband, A. M. Glazer, K. Roleder, A. Majchrowski and P. A. Thomas, *Journal of Applied Crystallography*, 2017, **50**, 378-384.

36. L. McGilly, D. Byrne, C. Harnagea, A. Schilling and J. M. Gregg, *Journal of Materials Science*, 2009, **44**, 5197-5204.

37. V. V. Shvartsman, B. Dkhil and A. L. Kholkin, *Annual Review of Materials Research*, 2013, **43**, 423-449.

38. R. Wang, B. Yang, Z. Luo, E. Sun, Y. Sun, H. Xu, J. Zhao, L. Zheng, H. Zhou, C. Gao and W. Cao, *Physical Review B*, 2016, **94**, 054115.

39. Z. Liu, Z. Luo, C. Wang, H. Wu, N. Zhang, H. Liu, W. Ren and Z.-G. Ye, *Ceramics International*, 2018, **44**, S189-S194.

40. Z. Liu, H. Wu, A. Paterson, Z. Luo, W. Ren and Z.-G. Ye, *Acta Materialia*, 2017, **136**, 32-38.

41. B. Noheda, J. A. Gonzalo, L. E. Cross, R. Guo, S. E. Park, D. E. Cox and G. Shirane, *Physical Review B*, 2000, **61**, 8687-8695.

42. D. E. Cox, B. Noheda and G. Shirane, *Physical Review B*, 2005, **71**, 134110.

43. Z.-G. Ye and M. Dong, *Journal of Applied Physics*, 2000, **87**, 2312-2319.

44. A. A. Bokov, X. Long and Z.-G. Ye, *Physical Review B*, 2010, **81**, 172103.

45. S. Gupta, S. Huband, D. S. Keeble, D. Walker, P. A. Thomas, D. Viehland and S. Priya, *CrystEngComm*, 2013, **15**, 6790.

46. L. M. Eng and H. J. Güntherodt, *Ferroelectrics*, 2000, **236**, 35-46.

47. J. Hlinka and P. Márton, *Physical Review B*, 2006, **74**, 104104.

48. R. Stumpe, D. Wagner and D. Bäuerle, *physica status solidi A*, 1983, **75**, 143-154.

49. O. Bidault, P. Goux, M. Kchikech, M. Belkaoumi and M. Maglione, *Physical Review B Condensed Matter*, 1994, **49**, 7868-7873.

50. D. O'Neill, R. M. Bowman and J. M. Gregg, *Applied Physics Letters*, 2000, **77**, 1520-1522.

51. C. C. Wang and S. X. Dou, *Solid State Communications*, 2009, **149**, 2017-2020.

52. T. Sluka, A. K. Tagantsev, P. Bednyakov and N. Setter, *Nature Communications*, 2013, **4**, 1808.

53. T. Sluka, A. K. Tagantsev, D. Damjanovic, M. Gureev and N. Setter, *Nature Communications*, 2012, **3**, 748.

54. B. M. Vul, G. M. Guro and I. I. Ivanchik, *Ferroelectrics*, 1973, **6**, 29-31.

Table 1. Atomic fractions of each element and calculated composition of 0.324BS-0.676PT crystal determined by EDX measurements.

	Pb^{2+}		Bi^{3+}		Sc^{3+}		Ti^{4+}		O^{2-}		
Area	Atomic %	Error %	Atomic %	Error %	Atomic %	Error %	Atomic %	Error %	Atomic %	Error %	Normalized Composition
#1	10.78	6.97	5.63	9.71	7.18	19.62	14.88	15.89	61.53	11.78	0.333BS-0.667PT
#2	11.18	6.24	5	9.61	6.71	19.33	14.56	14.57	62.55	10.98	0.313BS-0.687PT
#3	10.57	6.34	5.07	9.6	5.84	17.26	12.08	15.78	66.45	10.99	0.325BS-0.675PT
Averag	10.84(3)	/	5.23(3)	/	6.57(7)	/	13.84(0	/	63.51(0	/	0.323(7)BS-

e	)	)	0.676(3)PT

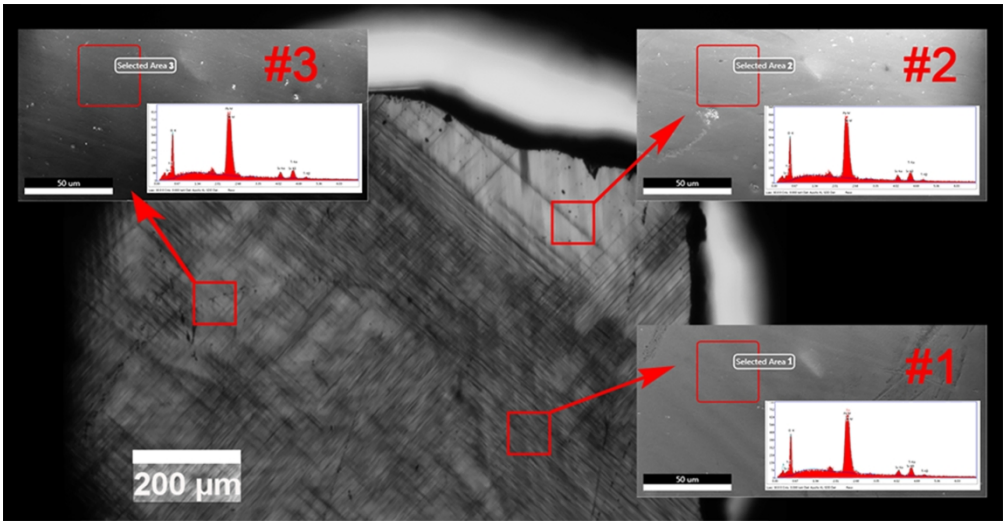

Figure 1. An polarizing light microscopy image of a $(001)_{cub}$ 0.324BS-0.676PT crystal platelet showing domains and the EDX spectra of the three different areas.

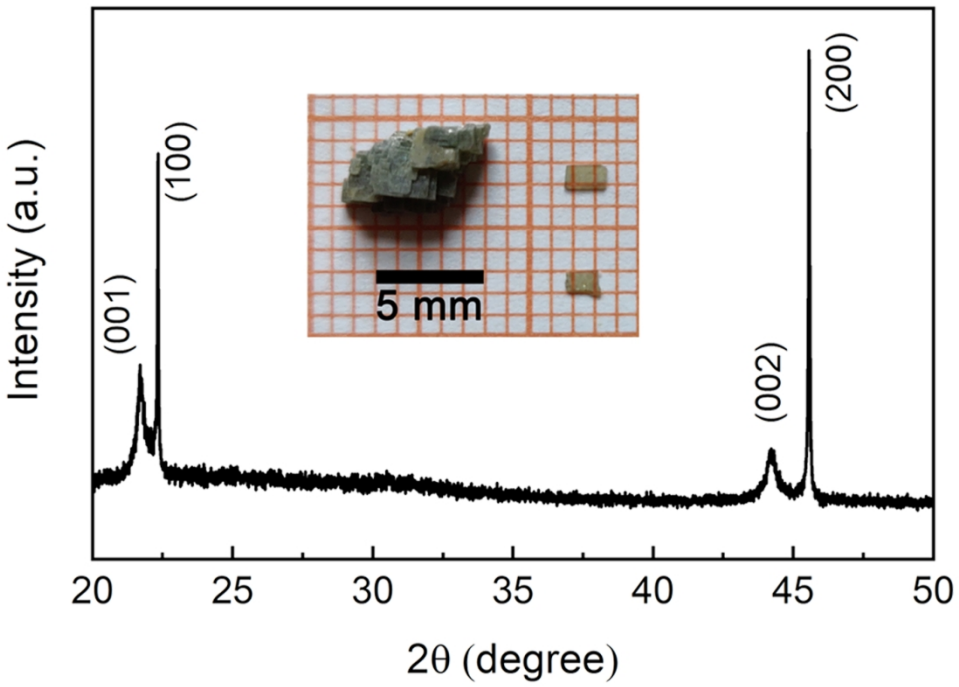

Figure 2. XRD patterns indicating the $\{001\}_{cub}$ facet of the 0.324BS-0.676PT crystal and an inset showing an image of the as-grown crystals and polished (001) platelets.

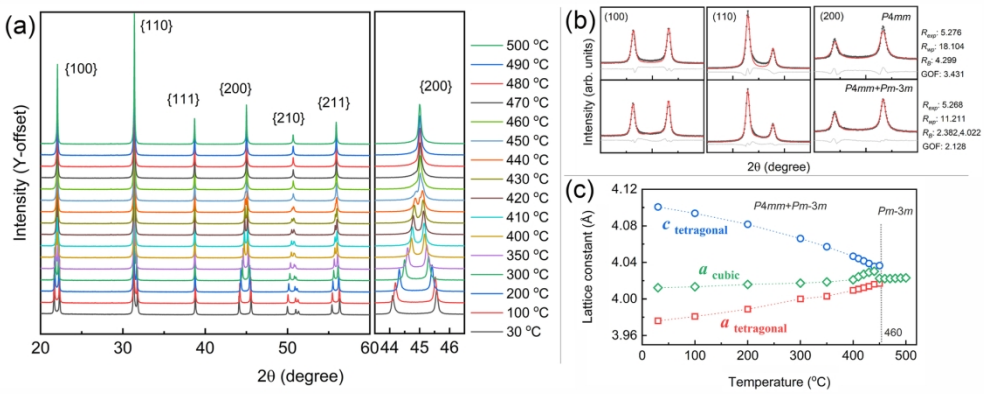

Figure 3. (a) X-ray diffraction patterns of 0.324BS-0.676PT crystals as a function of temperature indicating the temperature-driven structural phase transition. The gradual transformation to the high-temperature cubic phase is evidenced by the development of the {002} Bragg peak as a function of temperature. (b) Rietveld refinement results of the (100), (110), and (200) pseudocubic reflections at room temperature. (c) Variation of the Rietveld-refined lattice parameters as a function of temperature, confirming the tetragonal to cubic phase transition at T_C = 460 °C.

170x70mm (300 x 300 DPI)

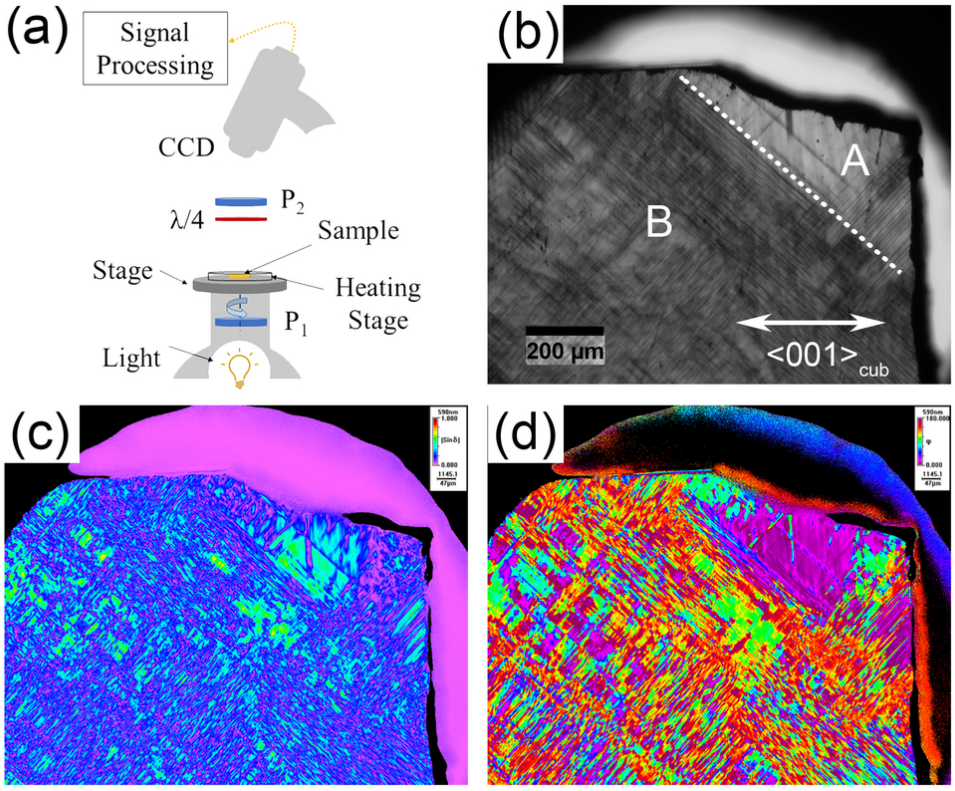

Figure 4. (a) Schematic of BIM setup showing the light path. (b) False colour image for transmittance (I_o) of a $(100)_{cub}$ 0.324BS-0.676PT crystal. (c) | *sin δ*| magnitude and (d) orientation images obtained at room temperature.

85x70mm (300 x 300 DPI)

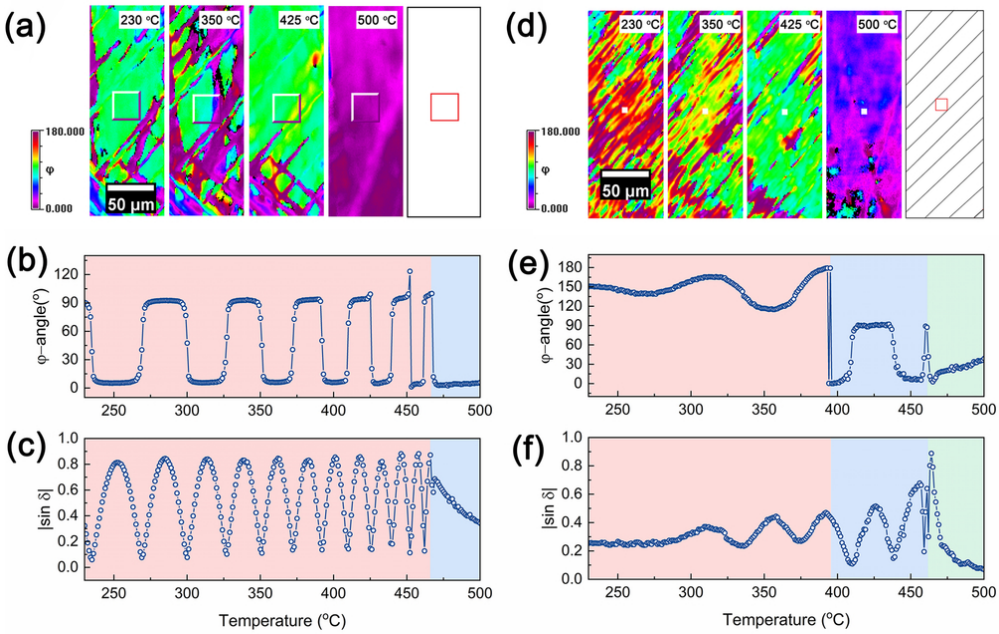

Figure 5. (a) and (d) Measured images of the orientation distributions of at 230, 350, 425, and 500 ^{o}C and the schematic presentations of the domain structures of a $(100)_{cub}$ 0.324BS-0.676PT crystal. The temperature dependence of the average orientations ((b) and (e)) and $|sin\ \delta|$ ((c)-(f)) of selected areas. The left-hand column and right-hand column refer to Part A and Part B, respectively, in Figure 4(b).

85x54mm (300 x 300 DPI)

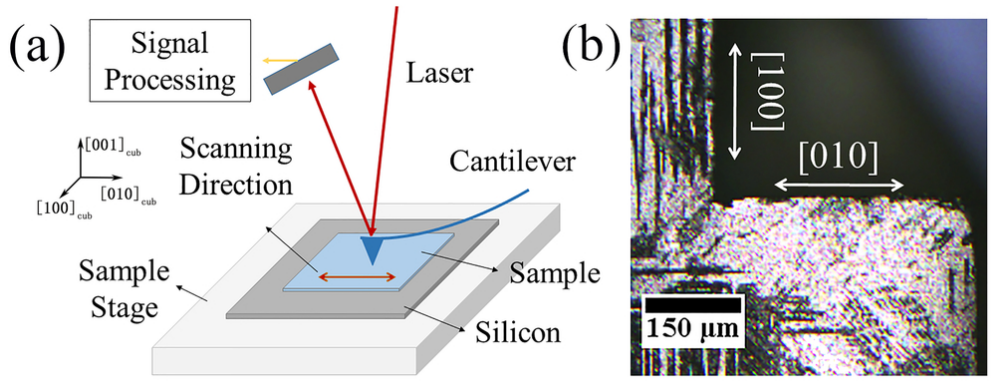

Figure 6. (a) Schematic of the PFM setup. (b) An optical image of the 0.324BS-0.676PT single crystal with as-grown facet captured by the PFM camera.

85x36mm (300 x 300 DPI)

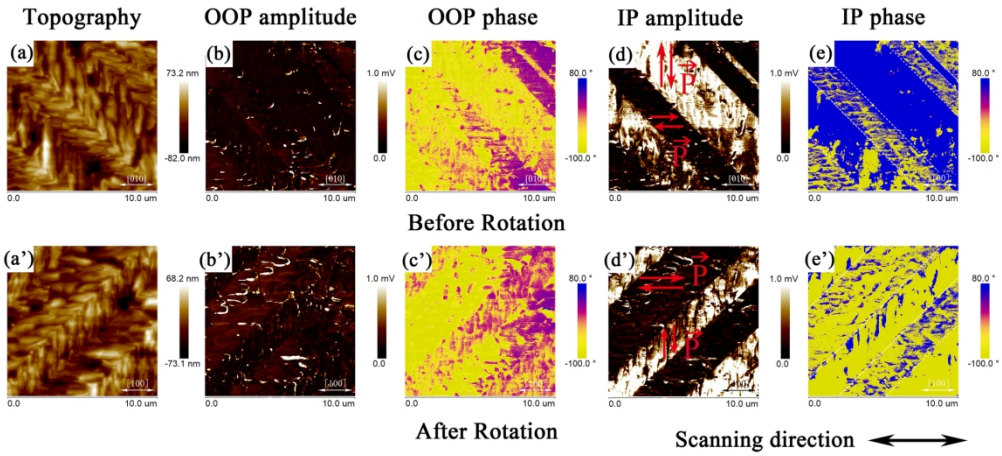

Figure 7. PFM images ($10 \times 10\,\mu m^2$ area) of a 0.324BS-0.676PT single crystal (imaging was performed using a tip voltage of 6 V, and a frequency of 45 kHz) obtained before rotation and after rotation: (a) and (a') topography, (b) and (b') out-of-plane (OOP) piezoresponse amplitude images, (c) and (c') OOP piezoresponse phase images, (d) and (d') in-plane (IP) piezoresponse amplitude images, and (e) and (e') IP piezoresponse phase images. The arrows in (d) and (d') indicate possible polarization directions in different domains.

170x80mm (300 x 300 DPI)

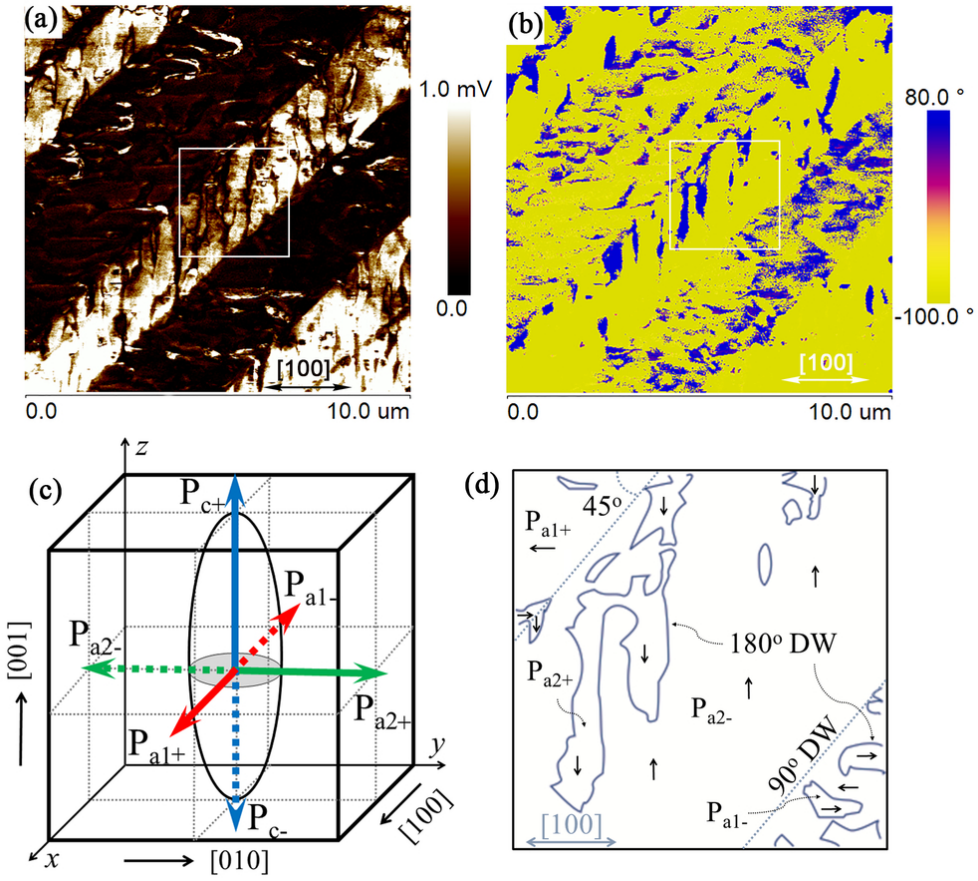

Figure 8. (a) and (b) In-plane piezoresponse amplitude image and phase image in Figure 7 (after rotation), respectively. (c) Orientations of 6 possible spontaneous polarizations and the optical indicatrix in a tetragonal phase. (d) Schematic domain structures of the selected area in Figure 8(a) (white square, $2.8 \times 2.8\ \mu m^2$).

85x75mm (300 x 300 DPI)

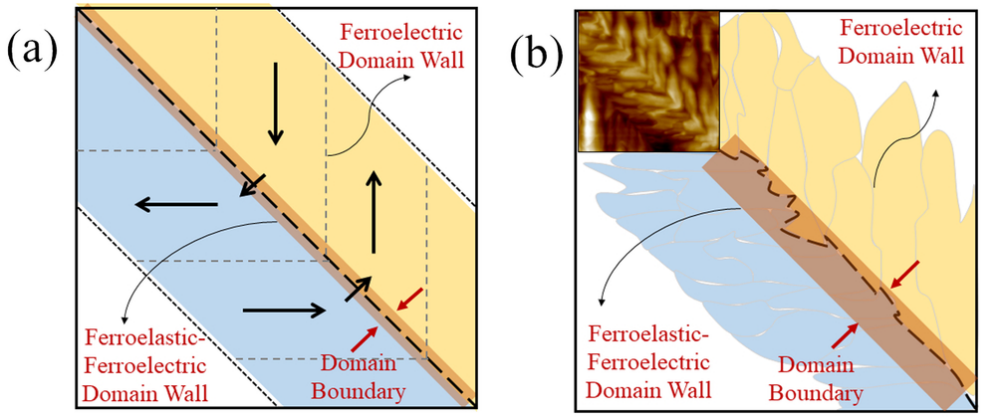

Figure 9. Schematics of head-to-tail, [110]-oriented, 90^{o} domain boundaries encountered in the BS-PT crystal. (a) Ideal polarizations in domains and in the boundaries are shown schematically by thick arrows; the orange stripe stands for the domain boundaries. (b) Schematics of the polarizations in the BS-PT crystal based on the topography image (inset) of PFM measurements.

85x36mm (300 x 300 DPI)

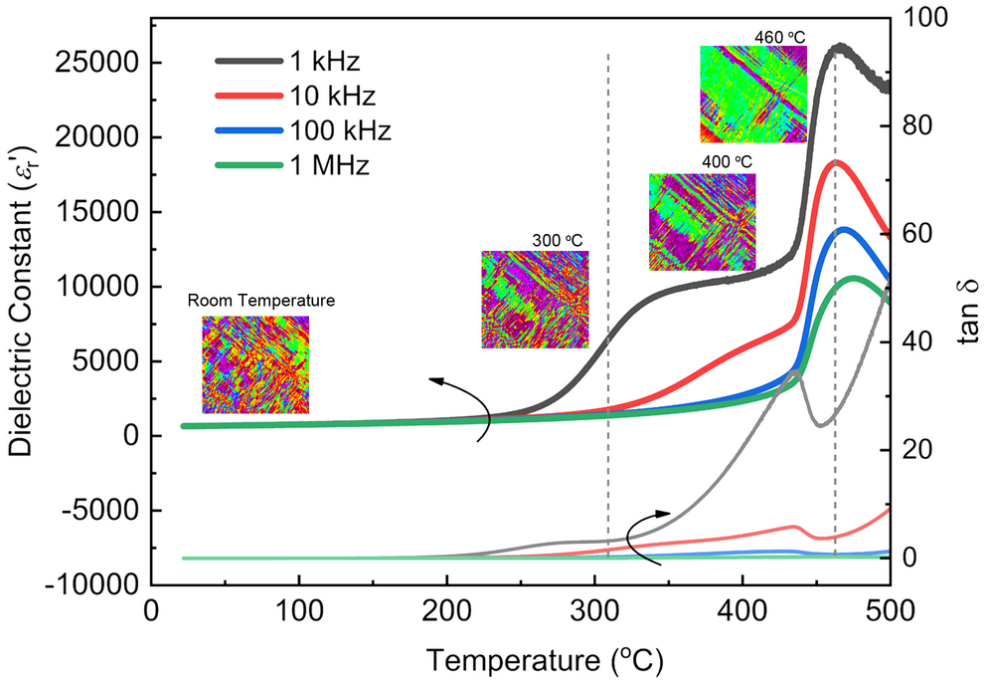

Figure 10. Variations of the dielectric constant and loss tangent of a (001) BS-PT crystal plate measured at various frequencies (1 kHz, 10 kHz, 100 kHz and 1 MHz) as a function of temperature, together with the domain structures (in the form of orientation images) obtained via BIM (200 × 198 μm^2) at selected temperatures.

85x59mm (300 x 300 DPI)

Table of Content

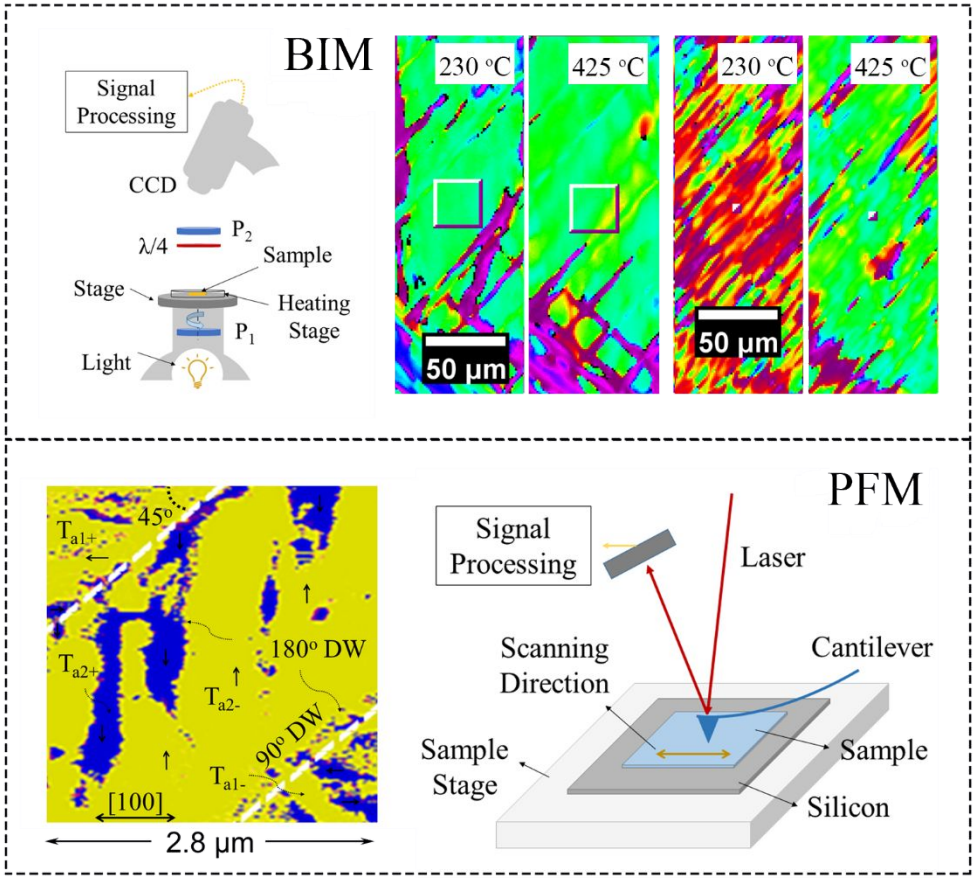

Multi-scale domain structures in the $BiScO_3$-$PbTiO_3$ single crystal are imagined and analyzed by Birefringence Imaging Microscopy (BIM) and Piezoresponse Force Microscopy (PFM), revealing the local crystal distortion in the vicinity of the domain walls.